Bulletin of Earthquake Engineering
https://doi.org/10.1007/s10518-025-02283-x

ORIGINAL ARTICLE

Seismic fragility assessment of high-rise tunnel-form buildings using a bespoke damage scale

Şahin Dede[1] · Tiziana Rossetto[1] · Fabio Freddi[1] · Ufuk Hancılar[2]

Received: 15 May 2025 / Accepted: 12 September 2025

Abstract
Tunnel-form buildings represent the main typology used in mass housing projects in Türkiye, with their heights continually increasing to meet the rising demand for land. Research has shown that low- and mid-rise tunnel-form buildings performed satisfactorily even under earthquake ground motions exceeding their design intensity. However, only a limited number of studies examined the performance of high-rise tunnel-form buildings. These structures are characterised by inherent vulnerabilities due to the use of lightly reinforced slender shear walls and conventionally reinforced squat coupling beams as primary structural members. The present study numerically examines the seismic performance of such structures and offers recommendations to enhance their design. A 14-storey tunnel-form building, representative of a large percentage of mass housing projects across Istanbul, is selected for case study purposes. A state-of-the-art three-dimensional non-linear finite element model is created in OpenSeesPY. Prominent failure modes of the components are incorporated into the model. The modelling strategy is validated at the component level using experimental results and at the system level using the results of ambient vibration tests conducted on an existing building. Standard and multi-mode adaptive pushover analyses are used to provide insights into the evolution of damage and define a damage scale. The seismic performance is evaluated through a Multiple Stripe Analysis procedure, and fragility functions are derived at both component- and system-levels. The fragility analysis shows that high-rise tunnel-form buildings have a very high probability of providing life safety even in very rare, high-intensity earthquakes. However, immediate occupancy of the building is likely to be jeopardised due to the severity of the incurred damage. The study offers several insights into the seismic performance assessment of such structures and provides guidance on how to improve their design.

Keywords Tunnel-form buildings · Shear walls · Coupling beams · Damage scale · Local engineering demand parameters · Seismic fragility curves

✉ Şahin Dede
sahin.dede.21@ucl.ac.uk

[1] Department of Civil, Environmental & Geomatic Engineering, University College London, London, UK

[2] Department of Earthquake Engineering, Boğaziçi University, İstanbul, Türkiye

Published online: 25 September 2025

1 Introduction

Reinforced concrete (RC) tunnel-form buildings have become increasingly popular in seismically active regions such as Türkiye. Tunnel-form buildings adopt a repetitive design and modular construction approach. Prefabricated steel formwork is used to create a mould for the walls and slabs of each bay of one storey. Each storey of the building is monolithically cast with concrete poured and cured onsite, reducing the number of cold-formed joints as compared to conventional construction methods. Following the hardening of concrete in one storey, the formwork is removed and reused in the construction of the storey above. The use of the same formwork allows for cost containment, and the repetitive nature of construction reduces the likelihood of faults due to human error. Moreover, when multiple structures are built at a site, construction of the storeys of each building can be phased such that the formwork is used across multiple structures whilst the concrete is curing, again increasing efficiency. Due to these advantages, tunnel-form construction is now the preferred building typology for mass housing projects sponsored by public bodies in Türkiye (Housing Development Administration of the Republic of Türkiye TOKİ 2022). Such buildings form a significant part of the urban fabric in cities such as Istanbul, Ankara, and Izmir. In Istanbul, more than 55,000 dwellings are housed in tunnel-form buildings constructed by the Istanbul Metropolitan Municipality (IMM) alone. Across the country, the primary public actor in mass housing, the Housing Development Administration of Türkiye (TOKI), has embarked on the construction of over one million housing units between 2002 and 2022, with tunnel-form buildings being the predominant typology (Housing Development Administration of the Republic of Türkiye TOKİ 2022).

This construction method yields a high density of shear walls, resulting in structures with high strength and stiffness. However, walls are generally slender and characterised by thin sections. Low- and mid-rise tunnel-form buildings showed 'good' seismic performance during the 1999 M_w 7.6 Kocaeli and M_w 7.2 Duzce Earthquakes in Türkiye e.g., (Yakut and Gulkan 2003; Balkaya and Kalkan 2003, 2004; Yüksel and Kalkan 2007; Kalkan and Yüksel 2008). More recent seismic events have confirmed the satisfactory performance of such structures but have highlighted several issues with high-rise structures comprising 10+ storeys. Following the 2023 M_w 7.7 and M_w 7.6 Türkiye earthquakes, a number of high-rise tunnel-form buildings were reported to be severely damaged (Dede et al. 2024), with a few collapsing (Sönmez and Rodriguez 2024). Dede et al. (2024) performed an extensive site investigation of a large set of high-rise tunnel-form buildings after the February 2023 Türkiye earthquakes. They reported consistent damage patterns, including extensive concrete crushing, reinforcement buckling, extensive damage to shear walls, and widespread brittle failure in coupling beams. Notably, the same damage patterns were observed following the 2010 M_w 8.8 Chile and 2011 M_w 6.2 Christchurch earthquakes in shear wall dominated high-rise buildings (Westenenk et al. 2012; Wallace et al. 2012; Massone 2013; Jünemann et al. 2015; Deger and Wallace 2015; Kam et al. 2011; Elwood 2013). Such structures resemble tunnel-form buildings as their seismic-resisting system is mainly based on lightly reinforced slender shear walls.

Further to post-earthquake observations, the seismic behaviour of tunnel-form buildings and similar slender shear wall systems has been investigated through a limited number of experimental studies. Yüksel and Kalkan (2007), Kalkan and Yüksel (2008) and Tavafoghi and Eshghi (2013) conducted quasi-static cyclic tests on 1/5 scaled four- and three-storey

tunnel-form buildings, respectively. Both studies highlighted the brittle failure of slender and lightly reinforced shear walls. Birely (2012) experimentally tested more than 60 slender (i.e., shear-span ratio > 2.0) and lightly reinforced shear walls that were designed to fail in tension according to the ACI 318–11 (American Concrete Institute 2011). The results highlighted that brittle mechanisms, such as concrete crushing, reinforcement buckling, and rupture, dominate the failure of these walls. Lee and Hwang (2013) performed shaking table tests and numerical simulations of a 1/5 scale 10-storey shear wall dominated system, highlighting that the high stiffness of these structures limits the effectiveness of coupling beams in dissipating seismic energy. Moreover, Yüksel and Kalkan (2007), Kalkan and Yüksel (2008) observed that the outer walls, in the direction of lateral load, resist the total moment by developing both tension and compression forces. This effect is due to the layout of the walls in the floor plan. Although it significantly contributes to the lateral load capacity, it generates complex interactions that might facilitate the formation of brittle failures.

Experimental and field observations on high-rise tunnel-form buildings have indicated a complex interaction between structural components, resulting in non-ductile local and system failures. The numerical simulation of such a response requires the development of highly sophisticated and experimentally validated models, along with the close monitoring of the local response of numerous structural components, resulting in a considerable computational cost. Constrained by these challenges, only a limited number of numerical studies exist, with only a subset representing high-rise tunnel-form buildings (see Table 1). Some of these studies (Lee and Hwang 2013; Ugalde et al. 2019; Gallardo et al. 2021) further highlighted the initiation of damage at low drift levels due to the high stiffness. Other numerical studies (Balkaya and Kalkan 2003, 2004; Ugalde et al. 2019) investigated the influence of slab modelling on the lateral stiffness and strength of these structures, demonstrating that the rigid diaphragm assumption is not suitable for tunnel-form buildings. In this context, Ramos and Hube (2021) demonstrated the importance of carefully calibrating the slab rigidity on the behaviour of shear wall structures with coupling slabs. The reviewed numerical studies also highlighted the occurrence of brittle failure in some shear walls. However, there is no consensus on the governing mechanism causing this failure. Some studies reported brittle failures due to bending moments (Yüksel and Kalkan 2007; Kalkan and Yüksel 2008; Lee and Hwang 2013; Odabasi et al. 2021), while others identified brittle failures under shear forces (Mohsenian and Di Sarno 2024). Finally, while all studies in Table 1 agree that coupling beams have an important role in the seismic response of high-rise tunnel-form buildings, there is no consensus on their contribution to energy dissipation. Some studies (Mohsenian and Di Sarno 2024; Behesthi Aval et al. 2018; Mohsenian and Mortezaei 2019; Mohsenian et al. 2021, 2024) report coupling beams failing before shear walls, while others (Lee and Hwang 2013) show the opposite.

Only a few studies investigated the influence of the ground motion (GM) uncertainty and derived fragility curves for tunnel-form buildings. These studies accounted for the record-to-record variability by performing Multiple Stripes Analyses (MSAs) or Incremental Dynamic Analyses (IDAs) and used peak ground acceleration (PGA), spectral acceleration at the natural vibration period ($S_a(T_1)$), or average spectral acceleration (avgSa) as Intensity Measures (IM) (Odabasi et al. 2021; Behesthi Aval et al. 2018; Mohsenian and Mortezaei 2019; Mohsenian et al. 2021, 2024). Many of the studies (Odabasi et al. 2021; Behesthi Aval et al. 2018; Mohsenian and Mortezaei 2019; Mohsenian et al. 2021, 2024) present fragility functions that adopt global response parameters, such as maximum interstorey drift

Table 1 Overview of key features of numerical studies on the seismic response of tunnel-form buildings

Study	Software	Structural System	Method	Key Features
Balkaya and Kalkan (2003, 2004)	POLO-Finite	Tunnel-form 2- and 5-storey	Pushover	- Tension-compression coupling of walls due to slab wall interaction is observed; - The rigid-diaphragm assumption was found to be unsuitable.
Yüksel and Kalkan (2007), Kalkan and Yüksel (2008)	DIANA^{+}	Tunnel-form 4-storey	Quasi-Static Cyclic	- Brittle flexural failure of shear walls observed; - Ductility of the boundary region is reported to be of high significance.
Lee and Hwang (2013)	Perform-3D	Shear wall 10-storey	Non-linear Response History	- Flexural wall damage starts at ~ 0.2% roof drift; - Damage in coupling beams occurs after the collapse prevention limit state is exceeded in the flexural and shear response of shear walls.
Ugalde et al. (2019)	Perform-3D	Shear wall 17- and 24-storey	Pushover and Non-linear Response History	- Maximum strength is reached at 0.6% and 1.0% interstorey drift; - It is concluded that the modelling of slabs has a pronounced effect on the stiffness and strength of the building.
Gallardo et al. (2021)	ANSYS	Shear wall 18-storey	Non-linear Response History	- Initiation of structural damage occurs at ~ 0.2% interstorey drift; - Localised and brittle damage in shear walls is observed.
Odabasi et al. (2021)	OpenSees	Tunnel-form 24-storey	Multiple Stripes Analysis	- Brittle flexural failure of shear walls is observed; - A substantially higher collapse risk of tunnel-form buildings compared to other tall building systems is reported.
Mohsenian and Di-Sarno (2024), Behesthi Aval et al. (2018), Mohsenian and Mortezaei (2019), Mohsenian et al. (2021, 2024)	Perform-3D	Tunnel-form 5- and 10-storey	Incremental Dynamic Analysis	- Shear failure is reported to dominate over flexural failure in shear walls; - An increasing influence of torsion on the seismic response is observed for the high-rise building; - Failure of coupling beams occurs prior to shear wall failure.

(MIDR) and maximum residual drift (MRDR), to represent the achievement of different damage states (DSs) in the buildings. Odabasi et al. (2021) derives fragility curves by using threshold values for these EDPs based on existing literature on structures other than tunnel-form buildings. In other studies (Behesthi Aval et al. 2018; Mohsenian and Mortezaei 2019; Mohsenian et al. 2021, 2024) the MIDR damage threshold values are derived by mapping global to local EDPs through non-linear static analyses (i.e., Pushover) and using the criteria in ASCE 7 (ASCE 2010) to assess component damage level. However, mapping MIDR threshold values from pushover analyses fails to incorporate torsional effects and overlooks the considerable differences in the responses between longitudinal and transverse directions in tunnel-form buildings. Moreover, the acceptance criteria in ASCE 7 overlook the specific characteristics of the typology. Finally, these studies do not present a numerical model validation, and make several modelling simplifications to reduce computational cost, such as

modelling slabs as rigid diaphragms (Odabasi et al. 2021) or using coarsely meshed fibre sections (Behesthi Aval et al. 2018; Mohsenian and Mortezaei 2019; Mohsenian et al. 2021, 2024), without accounting for the impact of these assumptions on the seismic response.

The present research work addresses the above-mentioned research gaps by adopting a sophisticated and validated numerical model of an existing tunnel-form building, which overcomes the modelling and analysis limitations of previous studies. A 14-storey tunnel-form building, typical of current mass housing projects in Istanbul, is selected for case study purposes. A three-dimensional non-linear Finite Element (FE) model of the case study structure is created in OpenSeesPY (Zhu et al. 2018). Existing literature and modelling strategies on the response mechanisms of slender shear walls and coupling beams are incorporated to capture the prominent failure modes of these members. The numerical model is validated at the system level against the results of ambient vibration tests, and at the component level against experimental data available in the literature. Standard and multi-mode adaptive pushover analyses are employed to provide insights into the evolution of damage at both component- and system-levels, leading to the proposal of a new damage scale specifically tailored to tunnel-form buildings. This damage scale adopts both local and global level Engineering Demand Parameters (EDP) for the definition of discrete DSs, which are successively used for seismic performance assessment through non-linear time history analyses. A Multiple Stripes Analysis (MSA) is conducted to examine the seismic vulnerability of the building over a wide range of GM intensities and to derive component and system-level fragility functions. The fragility functions are provided considering different IMs to facilitate the broader use of the results. The analysis results are critically discussed and compared with previous studies. This paper provides significant insights into the seismic response of high-rise tunnel-form buildings and highlights potential design improvements to enhance their seismic performance.

2 Case study structure and finite element modelling

2.1 Case study structure

Figure 1 shows the plan and elevation view of a typical tunnel-form building. According to the Istanbul Metropolitan Municipality, this particular design has been employed in the construction of high-rise tunnel-form buildings ranging from 12 to 15 stories across various locations in Istanbul. By 2023, it had facilitated the development of over 7,000 residential units. These buildings share the same structural properties, such as story height, floor plan, section dimensions, and reinforcement details. An existing building in Istanbul, with the same plan and elevation views (Fig. 1), is used in this paper for case study purposes. The building is a 14-storey residential building with one basement. It was constructed in Istanbul in 2010, and the authors were provided access to the building to conduct ambient vibration measurements, which were used for FE model validation, as discussed in Sect. 2.4.

The floor plan in Fig. 1 accommodates four dwellings and has 520 m^2 of floor area with a 6.44% shear wall area to floor area. Each story is composed of the same number of vertical elements and beams, including 26 shear walls, 12 columns and 27 beams. The slab is 15 cm thick, and the rest of the structural members have a constant 20 cm thickness due to the tunnel form's fixed formwork application. Beam heights are 45 cm and 60 cm. The total

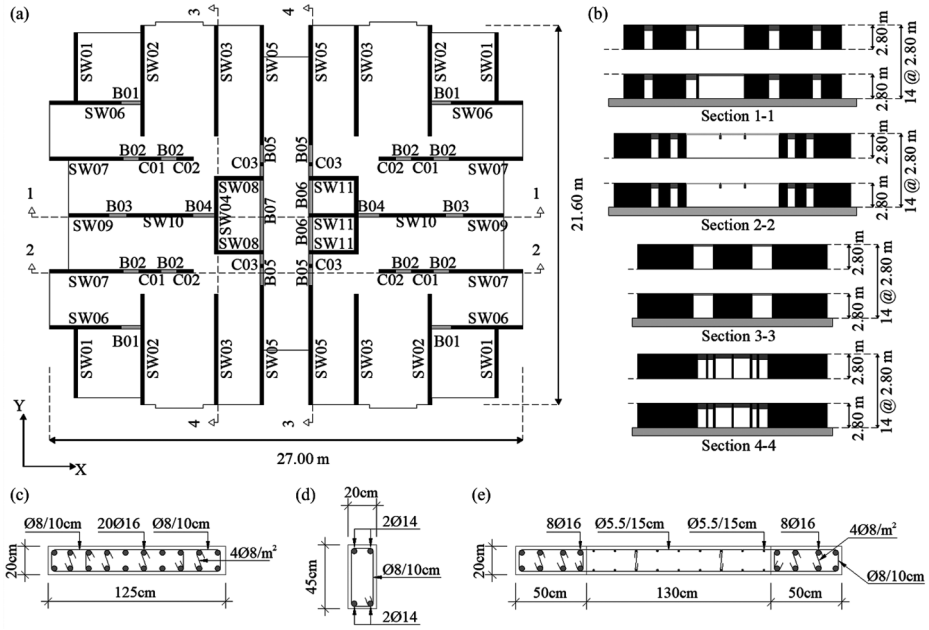

Fig. 1 (**a**) plan view of the case study tunnel-form building and nomenclature used for the structural members; (**b**) elevation view of the sections [units in m]; cross-sectional details of (**c**) column C01; (**d**) beam B01; (**e**) shear wall SW09

height of the building is 39.2 meters, and each story is 2.80 m in height, including the basement floor. All floors are architecturally identical except the basement, which is enclosed by continuous shear walls.

The seismic design was performed in accordance with the Turkish Building Seismic Code (TBSC 2007) (Ministry of Public Works and Settlement 2007). The reference structure is built on medium-dense soil and is located in the highest seismic zone of the 1996 seismic hazard map, i.e., with a PGA = 0.4 g. The seismic design forces were defined considering the design basis earthquake (i.e., 10% probability of exceedance in 50 years − 475-year return period) and high-ductility class (i.e., behaviour factor of 6). Concrete with compressive strength $f_c = 30$ MPa was used for all structural elements. Steel class BCIV, with a yield strength of $f_y = 420$ MPa, was used for the shear wall boundaries, columns, beams, and slabs. Steel class BCIIIa, with a yield strength of $f_y = 500$ MPa, was used as mesh reinforcement for the web sections of shear walls. Reinforcement details of the walls were calculated in accordance with the specifications provided for walls of high-ductile frame-shear wall (dual) systems, as no specific provisions were provided for tunnel-form buildings. Along the critical wall height, including ground- and first-story for the given building, shear wall reinforcements are denser than the rest. Slabs have mesh reinforcement at the top and bottom with varying diameters from 5.5 mm to 8.5 mm. Table 2 reports the reinforcement details of shear walls along the critical height, while Table 3 reports the details of beams following the nomenclature presented in Fig. 1. It can be observed that several walls are coupled through conventionally reinforced coupling beams with a span-to-depth ratio lower than 2.

Table 2 Properties of the planar shear walls

Member	l_w(m)	l_{wb}(m)	t_w(m)	$\rho_{wl,b}$(%)	$\rho_{wh,b}$(%)	$\rho_{wl,w}$-$\rho_{wh,w}$(%)	$cc_{w,s}$–$cc_{w,w}$(m)	Total number per storey
SW01	3.90	0.80	0.20	0.36	0.50	0.18	0.025–0.035	4
SW02	6.30	1.35	0.20	0.35	0.50	0.17	0.025–0.035	4
SW03	6.30	1.35	0.20	0.48	0.50	0.17	0.025–0.035	4
SW04	4.40	1.00	0.20	0.37	0.50	0.18	0.025–0.035	2
SW05	6.80	1.35	0.20	0.33	0.50	0.17	0.025–0.035	4
SW06	4.10	1.60	0.20	0.59	0.50	0.19	0.025–0.035	4
SW07	4.20	1.35	0.20	0.53	0.50	0.18	0.025–0.035	4
SW08	2.60	0.50	0.20	0.31	0.50	0.19	0.025–0.035	2
SW09	2.30	0.50	0.20	0.35	0.50	0.20	0.025–0.035	2
SW10	3.80	0.85	0.20	0.37	0.50	0.18	0.025–0.035	2
SW11	2.80	0.50	0.20	0.29	0.50	0.18	0.025–0.035	3

Note: l_w = wall length in plan; l_{wb} = wall boundary region length in plan; t_w = wall thickness; $\rho_{wl,b}$ = longitudinal reinforcement ratio of the wall's boundary; $\rho_{wh,b}$ = horizontal reinforcement ratio of the wall's boundary; $\rho_{wl,w}$ = longitudinal reinforcement ratio of the wall's web; $\rho_{wh,w}$ = horizontal reinforcement ratio of the wall's web; $cc_{w,s}$– $cc_{w,w}$ = clear cover along strong axis and weak axis, respectively

Table 3 Properties of the coupling beams

Member	l_b(m)	h_b(m)	t_b(m)	α_s	ρ_{bl}(%)	ρ_{bt}(%)	cc_b(m)	Total number per storey
B01	1.10	0.45	0.20	1.22	0.68	0.50	0.025	4
B02	0.90	0.60	0.20	0.75	0.96	0.50	0.025	8
B03	1.00	0.60	0.20	0.83	1.19	0.50	0.025	2
B04	1.20	0.60	0.20	1.00	1.19	0.50	0.025	2
B05	1.00	0.60	0.20	0.83	1.65	0.50	0.025	4
B06	1.90	0.45	0.20	2.11	2.44	0.50	0.025	2
B07	4.00	0.45	0.20	4.44	2.44	0.50	0.025	1
B08	0.60	0.60	0.20	0.50	1.65	0.50	0.025	4

Note: l_b = beam length in plan; h_b = beam height; t_b = beam thickness; α_s = span-to-depth ratio of the beam; ρ_{bl} = longitudinal reinforcement ratio of the beam; ρ_b = transverse reinforcement ratio of the beam; cc_b = clear cover

2.2 Finite element (FE) modelling

A 3D FE model of the case study building is developed in OpenSeesPY (Zhu et al. 2018). Figure 2 shows a schematic representation of the model along with the modelling details of different components. Line elements are used to represent shear walls, columns, and beams. For shear walls and wall-like columns, the wide-column analogy (Beyer et al. 2008) is adopted to model in-plane stiffness and provide a continuous connection with framing beams. To achieve these, section centroids of the shear walls are connected to the adjacent joints by stiff, elastic beams. The non-linear behaviour of walls, columns, and beams is simulated by a distributed plasticity approach through *'nonlinearBeamColumn'* elements in OpenSeesPY (see Fig. 2c and d). This is a fibre-based element that simulates the axial-flexural non-linear behaviour from the constitutive relationship of uniaxial material models located over the integration points, i.e., fibre sections. For the FE model of the case study building, the Gauss-Lobatto integration method is adopted for the section state determination (Scott 2011). The uniaxial behaviour of cover and core concrete is modelled through the *'Concrete01'* material model. The effect of confinement within the shear wall boundary

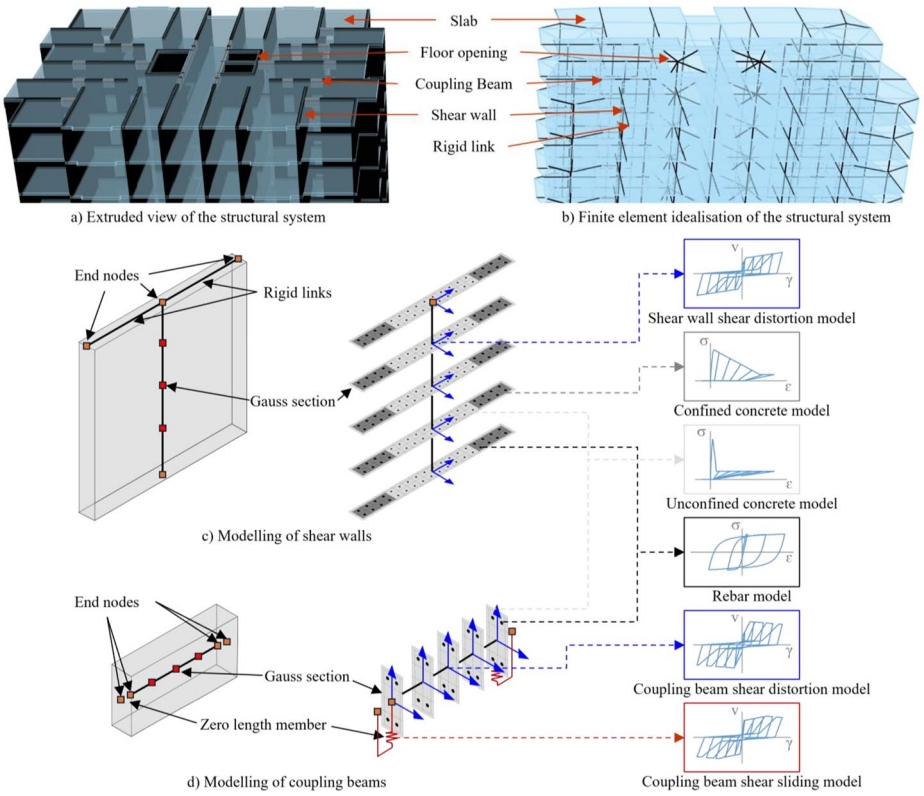

Fig. 2 Overview of the finite element (FE) modelling strategy for the case study frame

regions, beams, and columns is estimated based on Mander et al. (1988). The steel materials for both reinforcement classes are represented by the uniaxial *'Steel02'* material model with isotropic strain hardening in OpenSeesPY, which follows the work of Giuffré-Menegotto-Pinto (Filippou et al. 1983). The FE model also includes geometric non-linearities through the *'Pdelta'* coordinate transformation command.

Elastic membrane plate elements are used to model the slabs (see Fig. 2b). In line with standard practice, a factor of 0.25 is used to account for the reduction of effective bending stiffness in non-linear analyses (TBSC 2018 (Republic of Türkiye Ministry of Environment and Urbanization 2018), ACI 318 (American Concrete Institute 2011)). The perimeter shear walls enclosing the basement are modelled with '*ShellMITC4'*, and their effective bending stiffness is reduced by 0.50 as per TBSC 2018 (Republic of Türkiye Ministry of Environment and Urbanization 2018). Dead and live loads are assumed to be uniformly distributed over the floors. These are assigned to the joints of slab elements as point loads and to the beams as distributed loads. Masses are concentrated at the floor joints, and a Rayleigh damping matrix proportional to the mass and stiffness is used with a 5% damping factor. The developed FE model is validated at the local level against experimental data in the literature (see Sect. 2.3) and at the global level against the results of ambient vibration measurements (see Sect. 2.4).

2.2.1 Shear wall modelling

Modelling of local and global failure mechanisms in shear walls is critical to ensure the simulation of the seismic response of tunnel-form buildings (see Fig. 2c). Although a force-based distributed plasticity approach with fibre sections has significant advantages, this method cannot directly simulate certain failure types (e.g., brittle failure mechanisms) unless additional steps are taken. Concrete crushing, reinforcement buckling, and rupture are the primary failure modes in slender shear walls and cannot be simulated through fibre-based modelling unless modifications are applied at the material level (Pugh et al. 2015). Herein, flexure-dominated failure modes are incorporated into the uniaxial material relationships by forcing materials to sustain a total loss of strength when certain strain limits (Table 4) are exceeded. The crushing strain of concrete is assumed as the strain at which the compressive stress drops to 20% $(\varepsilon_{c,\,20})$ of the peak compressive stress. The buckling strain of reinforcing steel is taken equal to the crushing strain of the surrounding concrete. The rupture strain of the reinforcing steel is taken equal to 5%. Similar modelling strategies were used in previous studies (Ugalde et al. 2019; Gallardo et al. 2021; Gogus and Wallace 2015).

Deformation localisation is another critical issue to be considered when using the force-based formulation, although it is generally overlooked and not frequently adopted. Element integrals used in the force-based formulation generate localised strains at the base integration point, leading to a loss of objectivity in the post-peak response, which is more pronounced in the response of softening elements (Coleman and Spacone 2001). Pugh et al. (2015) noted that a softening-type response is frequently observed in RC shear walls, as they typically exhibit concrete crushing and/or reinforcement buckling at high drift levels. To prevent deformation localisation in shear walls and columns, the material regularisation procedure proposed by Pugh et al. (2015) is employed in this study. In this approach, the post-peak response of materials is modified considering fracture energy. It is worth mentioning that since the regularisation procedure affects the post-peak strength, strain limits explained in the previous paragraph are also modified to reflect the regularisation results.

Shear failures are simulated through an uncoupled trilinear shear force-deformation relationship included within the fibre sections through the *'section Aggregator'* command. Trilinear backbone curves are defined for each shear wall following the approach of Gogus and Wallace (2015) and are modelled through the uniaxial *'Hysteretic'* material. Cracking shear strength (V_{cr}) and ultimate strength (V_u) values are calculated per TBSC 2018 (Republic of Türkiye Ministry of Environment and Urbanization 2018) via the following Eqs. 1 and 2:

$$V_{cr} = \left(0.65 * 0.35\sqrt{f_{ck}}\right) * A_{ch} \tag{1}$$

Table 4 Limiting strain values applied to reflect material failures

Material	Failure Mode	Limiting Strain
S420 Class Reinforcing Bars (shear-wall boundaries, columns, and beams)	Rupture	+5.00%
	Buckling	−2.50%
Core Concrete - (Confined, $\varepsilon_{c,20}$)	Crushing	−2.50%
S500 Class Reinforcing Bars (shear-wall webs)	Rupture	+5.00%
	Buckling	−0.46%
Cover Concrete - (Unconfined, $\varepsilon_{c,20}$)	Crushing	−0.46%

$$V_u = A_{ch}\left[\left(0.65 * 0.35\sqrt{f_{ck}}\right) + (_{sh}f_{ywd})\right] \quad (2)$$

where f_{ck} is the concrete compressive strength, A_{ch} is the cross-sectional area, ρ_{sh} is the volumetric ratio of the transverse reinforcement, and f_{ywd} is the yield strength of the transverse reinforcement. Uncracked and cracked shear moduli are taken as $0.4E_c$ and $0.01E_c$, respectively, as recommended by Gogus and Wallace (2015), where E_c is the concrete's modulus of elasticity.

2.2.2 Coupling beam models

Coupling beams play a significant role in the seismic response and energy dissipation capacity of tunnel-form buildings. It is noteworthy that most existing tunnel-form buildings are characterised by squat coupling beams. Additionally, although such components are expected to support large shear forces and, in some cases, large inelastic deformations, they are often reinforced in a manner similar to ordinary beams. The shear span-to-depth ratio of coupling beams, α_s, ranges from 0.54 to 1.34. Experimental studies on short and conventionally reinforced coupling beams report that shear sliding and shear distortion significantly contribute to the member's total chord rotation, leading to a shear-dominated response (Breña and Ihtiyar 2011; Galano and Vignoli 2000; Kwan and Zhao 2002). Statistics of conventional RC coupling beam specimens provided by Ding et al. (2016) show four types of failure modes, such as shear tension, shear compression, shear sliding, and flexure.

The developed FE model uses *'nonlinearBeamColumn'* elements for all beams (coupling beams and other structural beams) (see Fig. 2d). These elements effectively capture the flexural response through the fibre sections but do not allow simulating shear mechanisms. Shear failure modes are captured through the model proposed by Ding et al. (2016). In this approach, two different backbone curves are incorporated into the fibre-based line elements to capture shear sliding and shear distortion modes. For shear distortion, a trilinear shear force-deformation backbone curve, defined through the '*Hysteretic'* material (Ding et al. 2016), is used to capture shear tension and compression failure. The stiffness of each branch, the cracking and the ultimate strength values are defined according to Ding et al. (2016), and the constructed backbone curves are aggregated at each integration point through the *'section Aggregator'* command. Conversely, shear sliding is represented through *'zeroLength'* elements at the members' ends (see Fig. 2d). These elements are characterised by a uniaxial response defined through trilinear backbone curves via the '*Hysteretic'* material model. Each coupling beam is analysed under monotonic loading, and shear force-slip backbone curves are obtained according to Eq. 3 (Ding et al. 2016):

$$\delta_{slip} = 200\left(\frac{V}{\sqrt{f'bh}}\right)\varepsilon_s^{0.7}\left(1 - \frac{A_{sm}}{A_s}\right)(unit : mm) \quad (3)$$

where ε_s is the maximum tensile strain of longitudinal rebars at the beam ends under the corresponding shear force V, and A_s and A_{sm} are the area of the total rebars and the additional longitudinal rebars near the centroidal axis, respectively. The obtained backbone curves are then approximated as trilinear curves and defined as the uniaxial response of *'zeroLength'* shear sliding elements. The interested reader can refer to Ding et al. (2016) for further details of the modelling strategy. As Eq. 1 was derived from a dataset of coupling beams

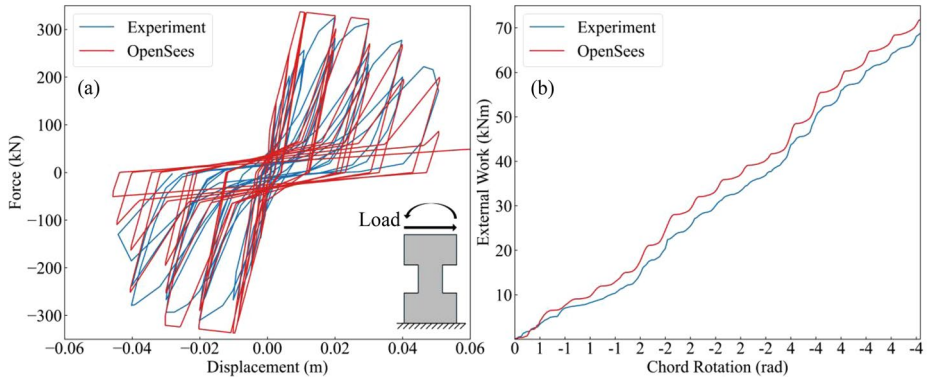

Fig. 3 Experimental and numerical comparison for beam specimen CCB1: (**a**) total hysteretic response; (**b**) external work

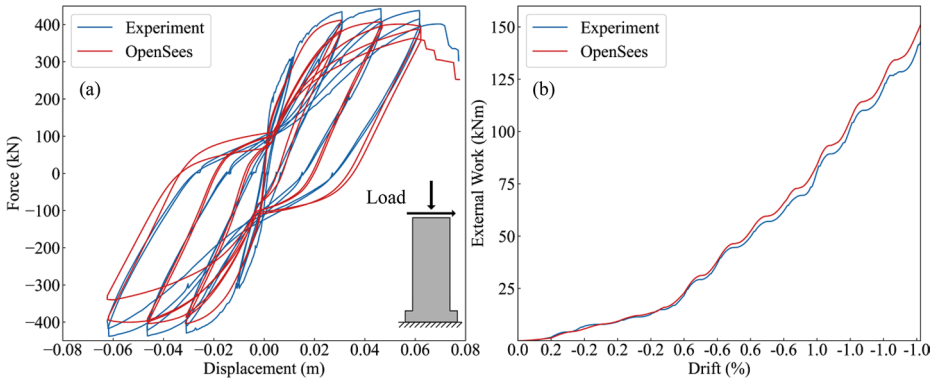

Fig. 4 Experimental and numerical comparison for shear wall specimen WSH4: (**a**) total hysteretic response; (**b**) external work

with α_s values lower than 1.83, shear sliding elements are not incorporated into beams with large aspect ratios ($\alpha_s > 2.0$), whose response is dominated by flexure.

2.3 Component-level validation

The numerical models for coupling beams and shear walls are validated against experimental results available in the literature. Figure 3 shows the comparison for a coupling beam specimen tested by Kwan and Zhao (2002), who report the cyclic behaviour of six half-scale models of deep RC coupling beams with maximum $\alpha_s = 1.0$. The comparison in Fig. 3 refers to the specimen CCB1, which is a conventionally reinforced coupling beam with $\alpha_s = 0.58$ exhibiting shear tension failure. Figure 3(a) compares the hysteretic response obtained by Kwan and Zhao (2002) in their experiments with that obtained for the same setup using the proposed modelling strategy. Figure 3(b) compares the experimental and simulated external work for 11 displacement cycles with chord rotations reaching up to 0.06 rad. Figure 4 presents the same graphs for a slender and planar RC shear wall sample, WSH4, tested by

Dazio et al. (2009). In all cases, the simulated responses show a satisfactory agreement with the experimental results, demonstrating the adequacy of the adopted modelling strategy. Additionally, Dazio et al. (2009) report concrete spalling and bar buckling starting at drifts of ~ 1.0%. The FE model shows the same material responses at approximately the same drift level.

2.4 System-level validation

At the system level, the FE model is validated against ambient vibration measurements of the reference structure. These measurements provide the dynamic properties of the system, such as dominant frequencies and torsion (Şafak et al. 2010), and allow validating the elastic dynamic response. The response of the case study building to ambient forces was recorded as accelerations at two different locations on the roof. Three-channel force-feedback Guralp Systems CMG-5T type accelerometers with a sampling rate of 100 Hz were deployed. Figure 5 shows the accelerometers and the monitoring system. Accelerometers were placed at the two opposite corners of the roof to capture the torsional response. This was essential as torsional response is one of the prominent aspects of tunnel-form buildings. The model validation is made considering the elastic version of the FE model in which the stiffness reduction factors described in Sect. 2.2 are neglected.

Figure 6 shows a 20-second-long snippet of the recordings. Ambient vibration data typically have very low signal-to-noise ratios (SNR) due to the low amplitude of the recorded response. This is more apparent in stiff structures and can distort the amplitudes and frequencies of the Fourier spectra. The autocorrelation operation is employed to overcome this possible issue. This process improves SNR as it amplifies the periodic components of the signal, and its use is suitable for stationary signals, e.g., ambient vibration data. Figure 7 shows the results of the Fourier spectral analysis conducted on the autocorrelation function, i.e., the power spectral density function (Şafak et al. 2010; Şafak and Çakti 2014; Kaya and Şafak 2015). The results show that the building's fundamental frequencies are around 1.7–2.0 Hz.

Band-pass filtering and detrending are applied to the raw data at each orthogonal direction. The obtained signals are then integrated to calculate the displacement histories given in Fig. 8(a) and (b) for East-West (EW) and North-South (NS) directions. The torsional component in Fig. 8(c) is then obtained by calculating the difference between the EW and NS displacement histories at Stations 1 and 2. Larger amplitudes of torsional displacements

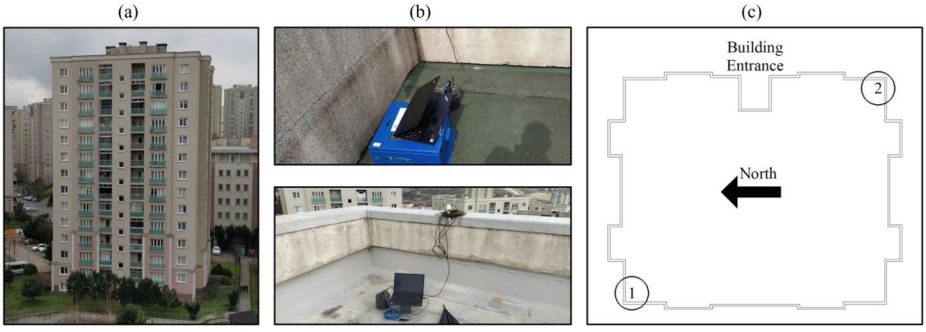

Fig. 5 Accelerometer deployment on the case study building

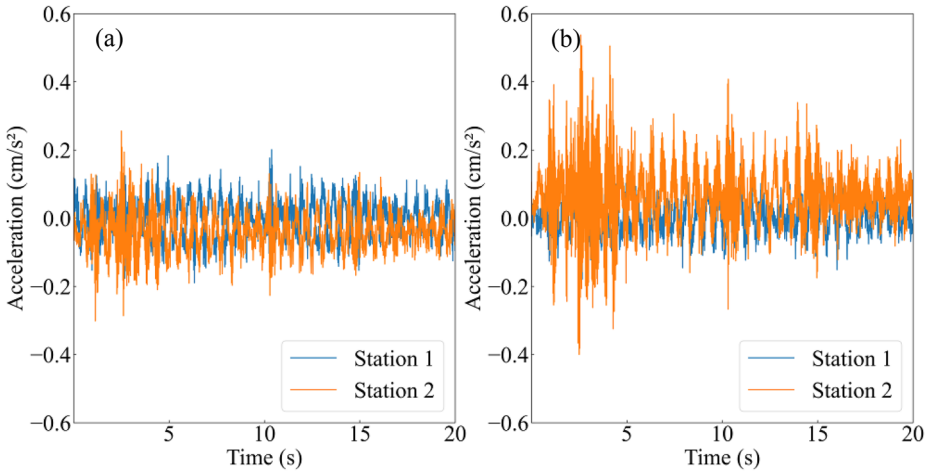

Fig. 6 Ambient vibration records along: (**a**) east-west direction; (**b**) north-south direction

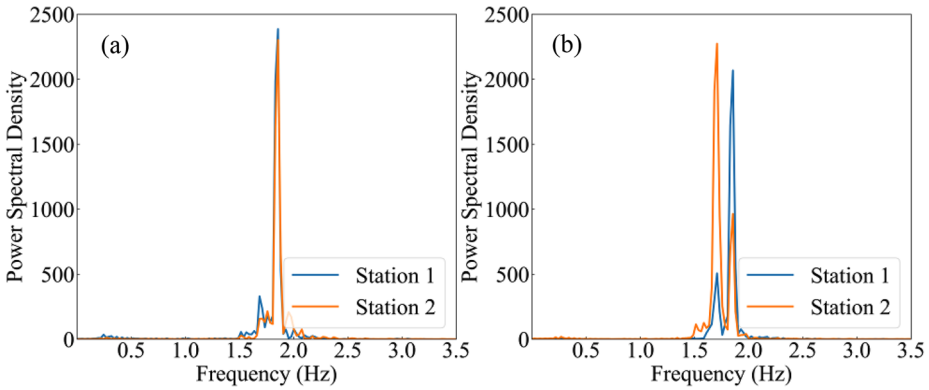

Fig. 7 Power spectral density function of vibrations along: (**a**) east-west direction; (**b**) north-south direction

compared to the translational ones indicate that the building exhibits torsional behaviour as the first mode's response. Between the two translational directions, the building exhibits larger amplitudes along the NS direction. This indicates that the second mode is along the NS direction and the third mode is along the EW direction, which correspond to the longitudinal and transverse directions of the building, respectively. Notably, as shown in Fig. 9, displacement histories along NS and EW have beat patterns at both stations, indicating that the second and third modes' natural period of vibration are very close.

Table 5 compares the fundamental periods obtained from ambient vibration data with those of the FE models. Fundamental periods of the FE model with gross section stiffnesses have shown good agreement with the fundamental periods obtained from the ambient vibration measurements. The first mode of the building is governed by torsional response, which is a salient property of this typology (Yakut and Gulkan 2003; Balkaya and Kalkan 2003,

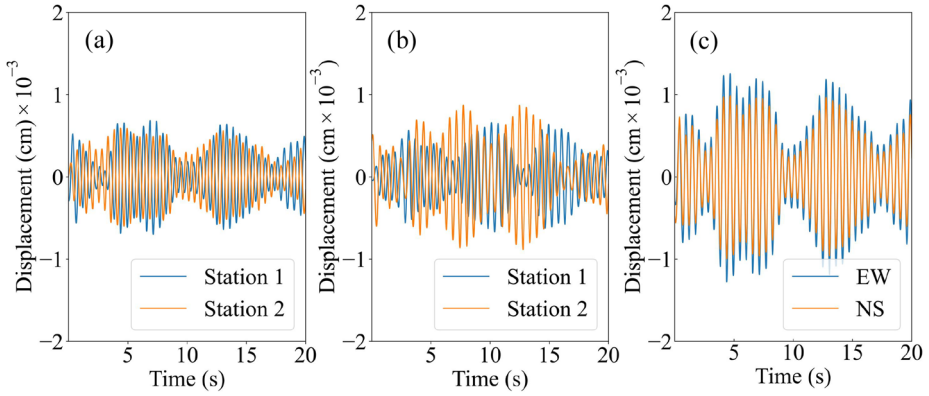

Fig. 8 (**a**) East-west direction translational displacement; (**b**) north-south direction translational displacements; (**c**) torsional displacements

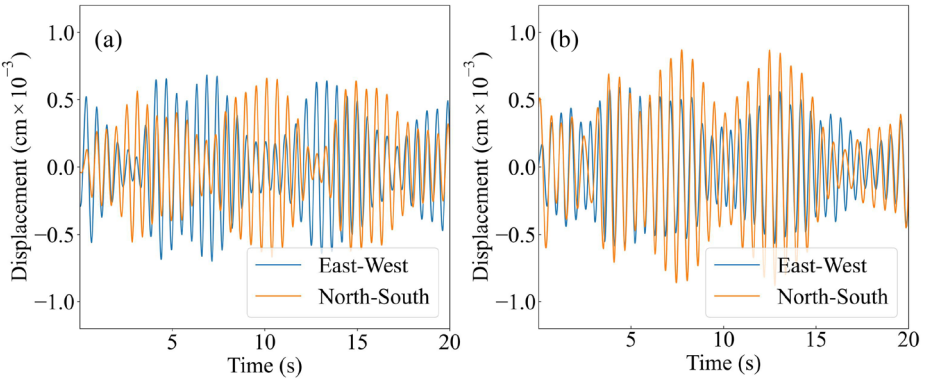

Fig. 9 Displacement response at: (**a**) station 1; (**b**) station 2

Table 5 Fundamental structural periods of the existing building and FE models

Mode	Response	Ambient vibration measurements (sec)	FE model with gross section stiffnesses (sec)	FE model with reduced section stiffnesses (see Sect. 2.2) (sec)
First	Torsional	0.58	0.58	0.64
Second	NS (X)	0.54	0.50	0.58
Third	EW (Y)	0.54	0.49	0.54

2004; Yüksel and Kalkan 2007; Kalkan and Yüksel 2008). The second and third modes of the building are translational and orthogonal modes with very close frequencies. Table 5 also reports the periods of the FE model with reduced section stiffnesses as described in Sect. 2.2. Non-linear response history analyses presented in the subsequent chapters are conducted on the FE model with reduced section stiffnesses.

3 Proposed damage scale for tunnel-form buildings

The seismic performance assessment is performed through a damage scale, defined to account for damage progression, failure modes, and redundancy. Tunnel-form buildings diverge from other RC systems, and, to the best of the authors' knowledge, there is currently no bespoke damage scale for this typology and damage scales of other typologies are not suitable to evaluate the performance of such structures. Existing damage scales either fail to provide quantitative damage state thresholds for a thorough performance assessment (Grünthal 1998), overlook the inherent redundancy in tunnel-form buildings (Ministry of Public Works and Settlement 2007; Republic of Türkiye Ministry of Environment and Urbanization 2018; Grünthal 1998), or fail to address the damage progression and brittle failure modes under flexural actions (ASCE 2010; Ministry of Public Works and Settlement 2007; Republic of Türkiye Ministry of Environment and Urbanization 2018; Hazus, FEMA 2022; Grünthal 1998). The proposed damage scale herein directly addresses distinctive features of tunnel-form buildings as it is defined based on the damage progression obtained from non-linear static analyses and monitoring multiple EDPs at both the material and component levels. The comprehensive monitoring of EDPs enabled the definition of discrete DSs with associated likely consequences.

3.1 Component limit states (CLSs) and engineering demand parameters (EDPs)

Damage in single structural components is herein characterised through the use of a number of Component Limit States (CLSs). These are described for coupling beams and shear walls in Table 6, and each CLS is deemed to have been reached when the associated threshold EDP is exceeded. A reference symbol is provided for each CLS, wherein the superscripts CB and SW indicate that the CLS is associated with coupling beams and shear walls, respec-

Table 6 Component limit states (CLSs) definitions

	Reference	Component Limit States (CLSs)	EDPs thresholds
Coupling Beams	CLS_1^{CB}	Start of shear cracks in the coupling beams	$\theta_{cr}{}^{*}$
	CLS_2^{CB}	90% of the coupling beam's ultimate shear strength is reached pre-peak	$\theta_{0.9u}^{pre\ *}$
	CLS_3^{CB}	20% drop in the coupling beam's ultimate shear strength post-peak phase	$\theta_{0.8u}^{post*}$
Shear Walls	CLS_1^{SW}	Cover spalling or bar yielding in the wall extremities	$\varepsilon_{cu}^{B} = -0.3\%$ OR $\varepsilon_{sy}^{B} = +0.2\%$
	CLS_2^{SW}	Confined concrete crushing or bar rupture in the wall boundary regions	$\varepsilon_{cc}^{B} = -2.5\%$ OR $\varepsilon_{su}^{B} = +5.0\%$
	CLS_3^{SW}	Unconfined concrete crushing or bar rupture in the wall web regions	$\varepsilon_{cu}^{W} = -0.5\%$ OR $\varepsilon_{su}^{W} = +5.0\%$
	CLS_4^{SW}	Diagonal shear failure of the shear wall	$\gamma_U = \pm 1.5\%$

Note: *Determined from cyclic analysis of each coupling beam; see Appendix A for values

tively. Instead, the subscript assigned to the CLS reference denotes the limit state number, with higher values corresponding to more severe damage.

For coupling beams, CLSs are defined with reference to experimentally observed responses of squat coupling beams (Breña and Ihtiyar 2011; Galano and Vignoli 2000; Kwan and Zhao 2002). CLS_1^{CB}, corresponds to the start of shear cracks, which is assumed to occur due to sliding at the beam-wall interface, distortion along the beam, or a combination of both, and is denoted by θ_{cr}. CLS_2^{CB} represents a situation near the maximum shear strength, and is characterised herein by the chord rotation at which 90% of the ultimate strength is reached, $\theta_{0.9u}^{pre}$, at the pre-peak stage. Experimental studies report that as the shear force approaches peak strength, the yielding of transverse reinforcements commences, and cracks widen at a faster rate. Therefore, at CLS_2^{CB}, the yielding of transverse reinforcement is expected to start. Furthermore, Kwan and Zhao (2002) reported the yielding of the main longitudinal reinforcements, occurring prior to the yielding of the transverse reinforcements, significantly changing the crack pattern and leading to a widening of cracks at the beam-wall interface. Hence, between CLS_1^{CB} and CLS_2^{CB} coupling beams are expected to exhibit extensive cracking both along the member length and at the beam-wall interface. After the peak strength is developed, coupling beams manifest rapid strength loss, and CLS_3^{CB} is reached at the chord rotation corresponding to 80% of the ultimate strength, $\theta_{0.8u}^{post}$, at the post-peak stage. As several designs are used for coupling beams in the case study structure, the specific chord rotation values defining the limit states are determined by conducting numerical analyses of the cyclic response of each coupling beam design. These values are presented in Appendix A.

For shear walls, material strains and shear deformation values are used to define the limit states at the material and section level. The use of material strains enables considering the variation in damage mechanism progression due to different section geometries, reinforcement detailing, and varying axial load levels. CLS_1^{SW} is defined as the first occurrence of either cover concrete spalling or longitudinal reinforcement yielding at the wall extremities. CLS_2^{SW} is defined as the first occurrence of either confined concrete crushing or longitudinal reinforcement rupture in the wall boundary regions. CLS_3^{SW} is defined as the first occurrence of unconfined concrete crushing or longitudinal reinforcement rupture in the wall web regions. The threshold values in Table 6 are derived from confined (ε_{cc}) and unconfined (ε_{cu}) ultimate strain of concrete, and yield (ε_{sy}) and rupture (ε_{su}) strains of the reinforcements of the case study structure's shear wall web and boundary regions (denoted with superscript W and B, respectively). Lastly, CLS_4^{SW} is defined as the diagonal shear failure, assumed to occur when the ultimate shear deformation (γ_U) for the section is reached.

3.2 Identification of global damage states (DSs)

Standard pushover analysis (i.e., with load pattern based on the first mode) is widely used in the seismic literature for the definition of DSs in building structures (e.g., Rossetto et al. 2016; Freddi et al. 2021). Although this approach is not strictly applicable to high-rise tunnel-form buildings, as it fails to incorporate the influence of higher modes and torsional effects, it can still provide valuable insights into the progressive development of local damages and associated changes in the system-level response. Table 7 presents a proposed damage scale for high-rise tunnel form buildings, based on the damage evolution observed from

Table 7 Damage States (DSs) definitions

Damage State	Damage State Description	Damage State Thresholds*	Consequence
No	No damage is observed.		No consequences.
Slight	Separation of infill walls from the surrounding structure. Plaster cracking and detachment is observed.	MIDR >0.2%	The building is immediately occupiable. Cosmetic repairs might be needed to fix non-structural damage. Repair of concrete cover or epoxy injection may be required to repair cracks in a few cases.
	Cover concrete spalling or bar yielding is observed in the extremities of a few shear walls.	CLS_1^{SW} is exceeded in more than 5% of shear walls at the ground floor.	
	Shear cracks are observed in a few coupling beams.	CLS_1^{CB} is exceeded in more than 10% of coupling beams at any floor.	
Moderate	Few infill walls fail.	MIDR >0.5%	The building is occupiable after some repair and minimal component strengthening. Epoxy injection or concrete replacement is required for the concrete cover of many shear walls, and a few may need some reinforcing bars replaced. Many coupling beams will require epoxy injection or concrete replacement, and a few may need to be replaced.
	Cover concrete spalling or bar yielding is observed in the extremities of many shear walls. Very few shear walls may suffer bar yielding, bar buckling or confined concrete crushing in their boundary regions.	CLS_1^{SW} is exceeded in more than 20% of shear walls at the ground floor.	
	Shear cracks are observed in many coupling beams. A very few coupling beams may fail in shear.	CLS_1^{CB} is exceeded in more than 20% of coupling beams at any floor.	
Extensive	In several shear walls, bar buckling, concrete crushing, and/or bar rupture are spread through the boundary region. Web damage or shear failure may be observed in a few shear walls.	CLS_1^{SW} is exceeded in more than 50% of shear walls at the ground floor. OR CLS_2^{SW} is exceeded in more than 5% of shear walls at the ground floor.	The building is not occupiable after the earthquake, and an extensive repair campaign is required to restore the building to its pre-earthquake condition. Many coupling beams require replacement. Many shear walls require significant repair and strengthening.
	Many coupling beams severely cracked and some fail in shear.	CLS_2^{CB} is exceeded in more than 30% of coupling beams at any floor. OR CLS_3^{CB} is exceeded in more than 5% of coupling beams at any floor.	
Near Collapse	Extensive cracks, bar buckling, and/or bar rupture are observed in the boundary regions of several shear walls reaching up to the web.	CLS_3^{SW} is exceeded in more than 20% of shear walls at the ground floor. OR CLS_3^{SW} or CLS_4^{SW} is exceeded in more than 5% of shear walls at the ground floor**.	Injuries due to infill wall failures are possible. The building is unsafe to enter following the earthquake. The building will likely need demolition.
	Shear failure is observed in a few shear walls.		
	Many coupling beams have failed in shear.	CLS_3^{CB} is exceeded in more than 30% of coupling beams at any floor.	

Note: * The first occurrence of any of the EDP thresholds indicates the entry of the structure into the DS; ** CLS_3^{SW} and CLS_4^{SW} are not necessarily sequential in the case of shear walls. Shear failure may occur independently from flexural failure.

pushover analyses. Each DS is described in terms of the typical damage that would be observed in the structural and non-structural components of the building, as well as the likely consequences in terms of building occupancy and the need for repair/demolition. DS thresholds are defined by the exceedance of MIDR values, which are indicative of non-structural damage in a storey, or by the exceedance of the CLSs (Table 6) in a percentage of structural components in a single storey. The percentage of damaged components associated with each DS is determined based on the extent and distribution of component-level damage that significantly alters the global response of the structure, as observed through pushover analyses. The proposed damage scale accounts for different modes of entry to each DS. A DS is reached when the first threshold is exceeded, regardless of the other damage mechanisms.

Entry to the *Slight DS* is conditioned on the first exceedance of any DS threshold provided for MIDR, ground-storey shear walls, and coupling beams. The pushover analyses show that the structure's lateral stiffness decreases at ~ 0.2% MIDR. This result is consistent with MIDR values indicating structural damage initiation in Gallardo et al. (2021). Up until this level, the pushover analysis shows that CLS_1^{SW} is exceeded in >~5% of ground story shear walls, where hairline cracks due to the yielding of longitudinal reinforcement are expected. The exceedance of CLS_1^{CB} in a few coupling beams is also expected due to the stiff and brittle nature of short coupling beams. In terms of consequences, damage to infill walls atypical of the *Slight DS* are likely to require cosmetic repairs. The limited structural component damage may require repair of the cover concrete or cracks. Hence, high-rise tunnel-form buildings in *Slight DS* can be considered equivalent to Grade 1 of EMS-98 (Grünthal 1998).

Entry to the *Moderate DS* is again conditioned on the first exceedance of any DS threshold provided for MIDR, ground-storey shear walls, and coupling beams. The pushover analyses show a sharp increase in the propagation of damage across the building in both shear walls and coupling beams after the analysis step, at which ~ 20% of ground story shear walls exceed CLS_1^{SW}. In light of this, entry to the *Moderate DS* is defined as the condition where CLS_1^{SW} is exceeded in more than 20% of ground-storey shear walls or CLS_1^{CB} is exceeded in more than 20% of coupling beams in any floor. The MIDR threshold is defined from the Eurocode 8 (CEN 2004) and represents a relative displacement at which some infill walls are likely to fail. In terms of consequences, tunnel-form buildings in this damage state are likely to have many shear walls requiring epoxy injection, and a few shear walls with larger cracks and spalled concrete needing concrete and bar replacement. Many coupling beams across multiple floors might require epoxy injection. Tunnel-form buildings in *Moderate DS* correspond to Grade 2 of EMS-98 (Grünthal 1998).

Entry to the *Extensive DS* is conditioned on the first exceedance of any damage state threshold provided for ground-storey shear walls and coupling beams. During the pushover procedures, *Extensive DS* is characterised by the near achievement of peak lateral strength. The pushover analyses show that this occurs when CLS_2^{SW} is exceeded in one ground story shear wall, which is seen to coincide with the exceedance of CLS_1^{SW} in ~ 50% of the ground story shear walls. Following the achievement of the peak lateral strength, damage to coupling beams becomes more severe and widespread, resulting in the exceedance of CLS_2^{CB} and CLS_3^{CB} in many coupling beams across multiple floors. Although substantial damage to structural components is observed in this DS, structural integrity is not jeopardised. Redundancy of the lateral load-resisting system inhibits the adverse impact

of severely damaged shear walls. This is in line with post-earthquake field reconnaissance observations (Kam et al. 2011; Elwood 2013; Lemnitzer et al. 2014). In terms of consequences, tunnel-form buildings in the *Extensive DS* need an extensive repair campaign due to the many severely damaged shear walls and coupling beams. Disintegration of concrete could be observed in coupling beams on multiple floors and also in the boundary regions of a few ground-storey shear walls. The expected repair cost and time are substantial (Ji et al. 2017; Li et al. 2019; Federal Emergency Management Agency FEMA 2018) and the building is unsuitable for immediate occupation. Tunnel-form buildings in *Extensive DS* can be considered equivalent to Grade 3 of EMS-98 (Grünthal 1998).

Lastly, entry into the *Near Collapse DS* is characterised by the loss of lateral strength, considerable sway, and snap-back type of response in the structure during the pushover analyses. These abrupt responses commence when more than two shear walls exhibit material failure in the web region. Reinforcement buckling and fracture occur in the boundary and web regions of shear walls, accompanied by the crushing of concrete, resulting in the exceedance of CLS_3^{SW}. Exceedance of CLS_3^{CB} occurs in the coupling beams across multiple stories, exhibiting diagonal and sliding cracks, as well as the disintegration of concrete. In terms of consequences, *Near Collapse DS* indicates that the building is unsafe to enter and that building demolition might be needed. Reinstating the building to its pre-earthquake condition will take considerable time and extensive strengthening efforts. Tunnel-form buildings in *Near Collapse DS* can be considered equivalent to Grade 4 of EMS-98 (Grünthal 1998), if the collapse has not occurred.

4 Seismic performance assessment

4.1 Intensity measure (IM) and ground motion (GM) selection

The selection of an appropriate IM is essential to establish a meaningful relationship between the hazard at the given site and the damage to the considered structure. The building presented in this study has a torsional first mode, has a non-negligible contribution of higher modes to its seismic response, and is expected to have period elongation under strong excitations. The geometric mean spectral acceleration (avgSa) is defined as the geometric mean of spectral ordinates at equally spaced periods. Readers may refer to Bianchini et al. (2009) for further details on the relevant equations. Several studies have demonstrated that avgSa exhibits less scatter over a range of periods than most conventional IMs, highlighting its suitability to account for higher mode effects and period shifts (Bianchini et al. 2009; Luco and Cornell 2007; Vamvatsikos and Cornell 2005; Cordova et al. 2000; Mehanny 2009; Kazantzi and Vamvatsikos 2015; Kohrangi et al. 2017). Furthermore, Kohrangi et al. (2017) demonstrated that avgSa is suitable for correlation with different EDPs. Given the mentioned advantages, avgSa is selected as the IM for deriving fragility functions. In this study, avgSa is calculated for ten distinct periods that are evenly distributed over the range of $0.2T_{1,min}$-$2.0T_{1,max}$. This period range is selected following the recommendations for shear-wall structures in (Haselton et al. 2012). The avgSa is adopted in the selection and scaling of earthquake records for the fragility analysis. However, the derived fragility functions are also provided in terms of peak ground acceleration (PGA) and spectral acceleration at the fundamental period of vibration ($S_a(T_1)$) to facilitate the use of the derived fragility

functions in risk studies that adopt more conventional hazard parameters. These fragility functions are presented in Appendix B.

As elaborated in Sect. 5, seismic fragility analysis is conducted through a MSA, in which twelve stripes are generated. Non-linear time history analyses are conducted for each of these stripes by applying 11 pairs of recorded GMs. Each pair is rotated 90 degrees to produce a total of 22 GM duplets per stripe. A total of 264 non-linear time history analyses are conducted. Care is taken to ensure that the pools of 11 records comprising each stripe are distinct from one another, in order to maximise variability between stripes. Furthermore, a maximum of three pairs of records of a single event are used in any of the GM pools to prevent a single event's dominance in any stripe. In total, 44 pairs of records are selected from the NGA2West (Ancheta et al. 2014) database for the MSA. These are selected for a source-to-site distance range of 20 km to 70 km, strike-slip fault mechanism, a magnitude range of $M_w = 5.0$ to $M_w = 7.5$ and soil $V_{s,30}$, range of 360 to 760 m/s. A ten-second zero-padding is applied to the end of each record to allow the building to undergo free vibrations and come to rest. The following chapter provides a detailed description of the building's response under two selected GM records from the aforementioned GMs pool.

4.2 Deterministic assessment

To provide detailed insights into the seismic behaviour of the case study building, this section compares the non-linear time history response of the structure subjected to the same GM scaled to two different IM values. For this comparison, the Iznik GM record of the $M_w = 7.5$ Kocaeli Earthquake of August 17th, 1999 is chosen, which was recorded on a site with a $V_{s,30} = 476$ m/s, at a distance of 30 km from the fault rupture. The GM is adopted with a scaled avgSa = 0.80 g and 0.47 g. To provide a basis of reference, avgSa values for the code-based uniform hazard spectra corresponding to GMs with 2475 and 475-year return periods are 0.93 g and 0.53 g, respectively. Although input motions do not precisely represent these code-based values, their proximity provides a means of comparison.

Modal analyses are conducted following the free-vibration phase at the end of each time history analysis. The comparison of the dominant mode of vibrations shows a considerable difference between the two cases. In the undamaged state of the building, the dominant natural vibration period of the long direction is 0.58 sec (Table 5). This value is elongated to 0.92 sec under the record with the higher avgSa and to 0.75 sec for the record with the lower avgSa. The periods of short direction are elongated to 0.63 and 0.59 sec from the initial value of 0.54 seconds, respectively. In both GM records, the mode of the long direction becomes the dominant mode, surpassing the torsional mode. Meanwhile, the mode of the short direction remains the third mode as in the initial state. The fact that the highest inelastic period lengthening occurs in the mode of long direction agrees with the pushover results, indicating that the building is likely to sustain more severe damage in the long direction. The MIDR profiles in Fig. 10 also indicate the contribution of the coupling beams in the long direction as the building shows a frame-like MIDR profile.

The results show that the building suffers inelastic deformations under both GMs (see Fig. 11). As expected, the severity of damage is lesser under the GM with the lower avgSa. In this case, 40% of ground story shear walls exceed CLS_1^{SW} and only one coupling beam in the whole building exceeds CLS_1^{CB}, making the building enter the *Moderate DS* (Table 7). Based on the previously mentioned proximity of this case with 475-year return period

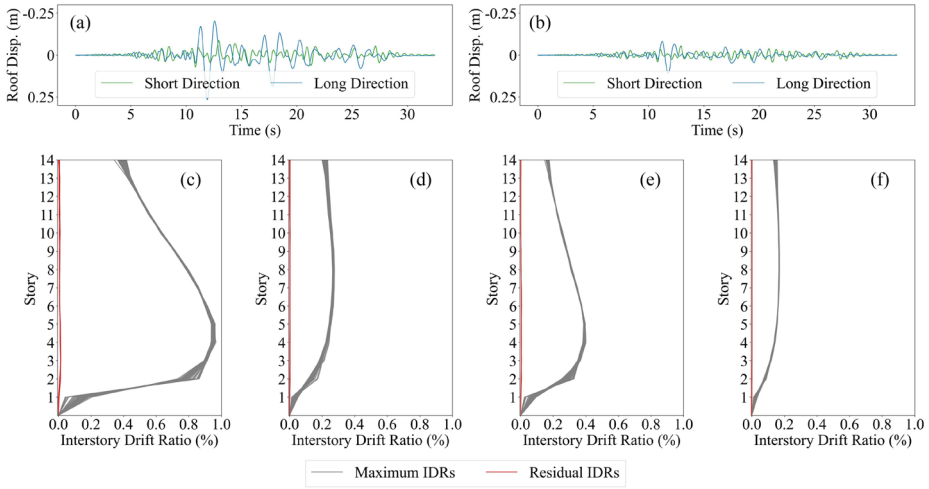

Fig. 10 Global response: (**a**) roof displacement, higher avgSa; (**b**) roof displacement, lower avgSa; (**c**) MIDR profile of the long-direction, higher avgSa; (**d**) MIDR profile of the short-direction, higher avgSa; (**e**) MIDR profile of the long-direction, lower avgSa; (**f**) MIDR profile of the short-direction, lower avgSa

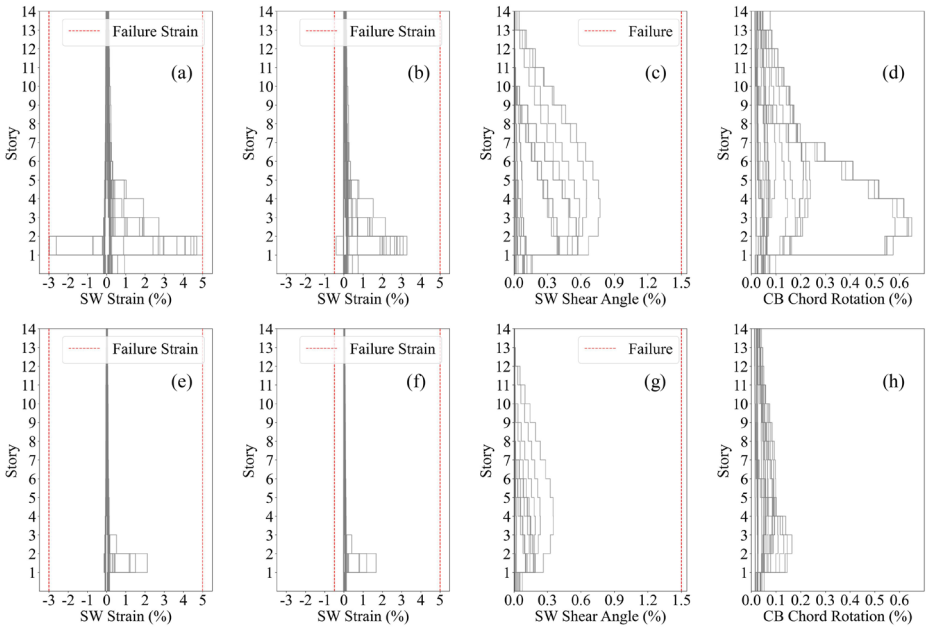

Fig. 11 Component response: (**a**) Strain in the outermost layers of shear wall boundary regions, higher avgSa; (**b**) Strain in the outermost layers of shear wall web regions, higher avgSa; (**c**) Shear angle in shear walls, higher avgSa; (**d**) Chord rotations in coupling beams, higher avgSa; (**e**) Strain in the outermost layers of shear wall boundary regions, lower avgSa; (**f**) Strain in the outermost layers of shear wall web regions, lower avgSa; (**g**) Shear angle in shear walls, lower avgSa; (**h**) Chord rotations in beams, lower avgSa

code-based spectrum, the building exhibits a good performance. The damage is much greater under the GM with the higher avgSa, with several shear walls observed to fail in tension and compression zones. In this case, the ground story shear walls suffer the most damage: bar rupture occurs in one T-shaped shear wall's boundary region, high strain demands are incurred in several planar shear walls, the crushing of confined concrete in a few planar shear walls' boundaries, and softening of unconfined concrete in the web region of one planar shear wall. The examination of the case with the higher avgSa, therefore, shows that the building falls into *Extensive DS* (Table 7). An important observation made through residual interstorey drifts in Fig. 10 is that the building recovers its pre-earthquake position despite the inelastic deformations in several shear walls. This points to the high redundancy of the typology as similar observations were made on an instrumented shear wall dominant building during the aftershocks of the 2010 Chile earthquake (Lemnitzer et al. 2014).

Results of the GM with the higher avgSa also show that almost all of the critical damage occurs in the shear walls extending parallel to the long direction and located on the outermost edges of the ground floor. This observation agrees with the findings of Kalkan and Yüksel (2008), Yüksel and Kalkan (2007), who highlight the importance of tension-compression coupling at the structural level that occurs due to the slab-wall interaction. Among the damaged ground-floor shear walls, four have identical sections (SW07). These walls experience axial tension forces of approximately 10% P/f_cA and axial compression forces between 40%-50% P/f_cA, and suffered tensile strains reaching 4%, where P is the axial force, A is the gross section area, and f_c is the concrete compressive strength. Another shear wall (SW09), which suffered significant softening of unconfined concrete in the web region, was subjected to an axial compression force of 87% P/f_cA. It should be emphasised that these shear walls under high levels of axial forces are part of coupled wall systems, and the results indicate the effectiveness of the load transfer mechanism since the axial forces on shear walls are the cumulative sum of shear forces attained by the connecting coupling beams. However, the results also show a total failure of capacity design principles.

Figure 11(d) and (h) show that induced chord rotations in coupling beams are low for both GMs, with the majority remaining below CLS_1^{CB} and none exceeding CLS_2^{CB} under the GM with the higher avgSa. These results indicate that the ductility of the coupling beams is not properly utilised to dissipate energy, with the shear walls instead suffering damage and having a higher likelihood of brittle failure due to the high axial loads. The contribution of the coupling beams to the energy dissipation may be inhibited by the high overall stiffness of the shear-wall system, which limits interstorey deformations and, therefore, the imposed chord rotations on the coupling beams. The very stiff response of the building tends to soften through the damage incurred in the shear walls. These results agree with the findings of Lee and Hwang (2013), who, based on shake-table test observations, states that coupling beam damage commences after severe damage of the shear walls.

Figure 11(c) and (g) show that shear walls' deformations are less than the diagonal shear failure limit. As stated in Sect. 2, the shear response is decoupled from the flexural response in the numerical model. Therefore, any incurred damage under flexural actions is not transferred into the shear response. The results show that shear deformations are considerably lower than the failure threshold (CLS_4^{SW}), even in the most severely damaged shear walls. Furthermore, flexural deformations are not seen to spread vertically in the shear walls. Hence, shear deformations are not expected to jeopardise the vertical components in this

case study structure, and these results suggest that decoupled modelling of shear response is sufficient for the case study building as shear demands remain low.

Out-of-plane buckling of slender shear walls, which occurs due to the loss of stability in the flexural compression zone, is a brittle failure mechanism that cannot be simulated within the adopted modelling methodology. Results show that crushing of confined concrete occurs in the compression zone of several shear walls, and in one wall, this damage spreads further into the web. Complete crushing of the cover concrete results in a 30% loss in section thickness, as the depth of clear cover is 3.5 cm on each face in the weak axis of the walls, and a significant increase in the slenderness ratio. Moehle (2015) recommends $l_u/b \leq 10$ within the intended hinge region, where l_u is the clear story height and b is the wall thickness. This ratio is 14 in the case study building's initial state and increases under the loading reversals due to the development of cover crushing. Therefore, the stability of the flexural compression zone is compromised in the first loading case.

5 Seismic fragility analysis

Following the deterministic assessment, the results of MSA are examined to establish statistically meaningful relationships based on corresponding EDP-IM pairs. This study employs the MSA method to establish the relationship between different EDPs and the selected IM. GM records are scaled to obtain specific IM values at each stripe, such that multiple stripes of EDPs corresponding to specific IM values are produced from the subsequent non-linear time history analyses (Jalayer 2003). Herein, twelve avgSa values, representing twelve stripes, are defined using code-based uniform hazard spectra (UHS) corresponding to 43-, 72-, 475-, and 2475-year return periods. A mean elastic response spectrum for each avgSa value is generated by scaling 11 pairs of GM records in the time domain. As shown in Fig. 12, the range of mean elastic response spectra covers the four code-based UHS and sufficiently matches their shape.

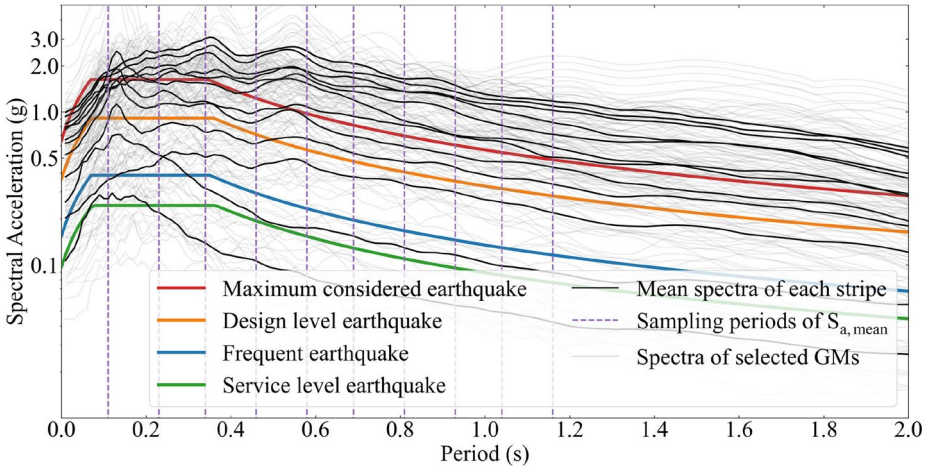

Fig. 12 Seismic inputs

Figure 13 illustrates the maximum-over-time demand values of the selected EDPs among all shear walls, and across the avgS$_a$. Figure 13(a) and (b) display a sharp jump in the boundary and web strain, following the sixth stripe. This sharp change coincides with the start of cover concrete failure, indicating the rapid failure of the compression zone following the loss of cover concrete. These results generalise the observations made in Sect. 4.2. In addition, samples of failed concrete and steel fibres lie outside the 5th and 95th percentile limits of the distribution of recorded peak strains, indicating that damage is concentrated in only a few locations and again agrees with the field observations. This observation also justifies the decision to base the DS definitions in Table 7 on proportion of components damaged in one storey, i.e., the ability to capture concentrated damage in the system. Furthermore, upon examination of the coupling beams, it is found that the observations made during the deterministic assessment are consistent across all GMs. Unless significant damage is incurred in shear walls, that impose chord rotation on coupling beams, the damage to coupling beams remains limited.

Component-level fragility curves presented in Fig. 14 illustrate the probability of exceedance of the CLS presented in Table 6. To generate the data for the fragility curves, the time-history response of each component in the structure is considered separately, and CLS exceedance is checked. The fragility functions are derived assuming that EDPs follow a lognormal distribution and adopting the maximum likelihood method for the fitting of the obtained results (Baker 2015). The comparison of Fig. 14(a) and (b) shows that coupling beam damage occurs after yielding of the outermost bars in the shear walls. Following damage to at least one coupling beam, boundary damage to the shear walls commences in the

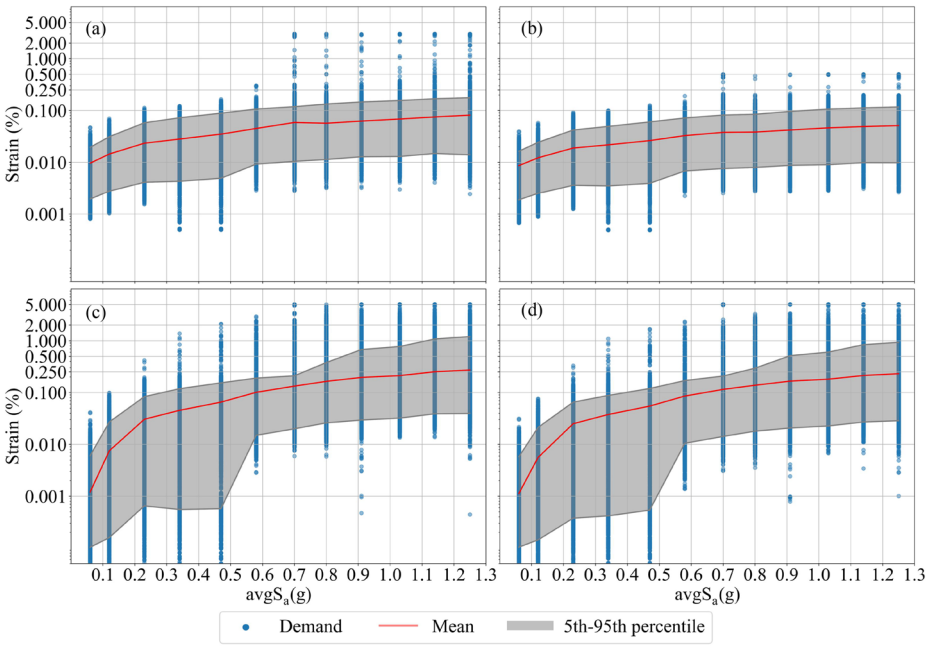

Fig. 13 Demands on shear walls and corresponding limit states: (**a**) strain of the confined concrete fibre at the outermost end of the boundary regions; (**b**) strain of the unconfined concrete fibre at the outermost end of the web regions; (**c**) strain of the steel fibre at the outermost end of the boundary regions; (**d**) strain of the steel fibre at the outermost end of the web regions

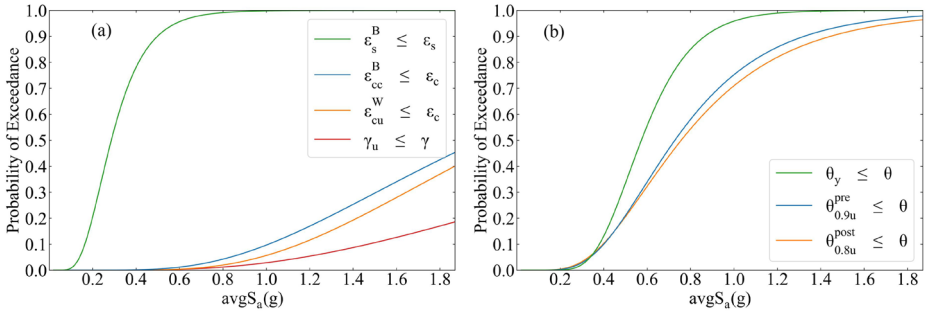

Fig. 14 Component-level fragility curves for: (**a**) shear walls; (**b**) coupling beams

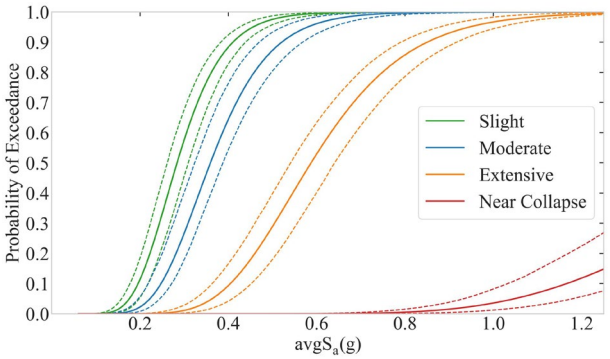

Fig. 15 System-level fragility curves

form of the crushing of confined concrete. Damage to the web region of shear walls occurs, manifested as crushing of unconfined concrete, and is followed by failure under shear deformations. The component-based fragilities, therefore, agree with the damage progression observed during the pushover and deterministic analyses.

Figure 15 shows the mean system-level fragility curves as a function of avgSa, along with the associated 95% confidence intervals (CIs), illustrating the exceedance probabilities of discrete DSs defined in Table 7. CIs in Fig. 15 are constructed using a bootstrap analysis where fragility functions are fitted to 1000 sets of new values of DSs that are generated for the available IMs. Interested readers can refer to Rossetto et al. (2014) for a thorough discussion of the application of bootstrap analysis to fragility functions. In addition to avgSa as the IM, system-level fragility curves and associated CIs are derived as a function of $S_a(T_1)$ and PGA (see Appendix B), utilising the same GM pool. Comparison of the system-level fragility curves and associated CIs in Figs. 15 and 16 suggests that estimated fragility parameters through avgSa pose a lower uncertainty across all DSs compared to those estimated through $S_a(T_1)$ and PGA, as narrower confidence intervals are obtained.

Figure 15 illustrates that the case study building has a good seismic performance even under very rare earthquakes. Considering avgSa value of 2475-year return period code-base spectrum (0.93 g), results show that the building has 3% mean exceedance probability of the *Near Collapse DS*. This indicates that the case-study building has a very high probability of providing life safety even in very rare events, although severe damage to the building is expected considering the mean exceedance probability of *Extensive DS* under

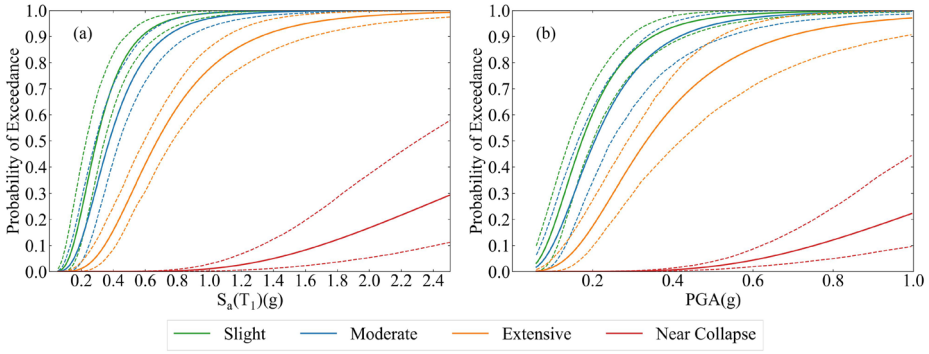

Fig. 16 System-level fragility curves as a function of: (**a**) $S_a(T_1)$; (**b**) PGA

the same earthquake. The building is expected to suffer from severe boundary damage in ground-story shear walls, requiring a significant repair campaign to recover the building's pre-earthquake condition. Whereas, if the design earthquake is considered (avgSa = 0.53 g), it is found that the building is very likely to require repair and minimal component strengthening while maintaining its occupancy.

It is important to note that damage to the ground-story shear walls is the determining factor governing entries into each DS. However, significant damage to coupling beams occurs in multiple floors under higher values of avgSa, as shown in Fig. 14. This supports the aforementioned observations regarding the poor effectiveness of coupling beams in dissipating the seismic energy. However, their impact on the post-earthquake occupancy of the building grows rapidly beyond avgSa of 0.6 g as a consequence of the likely repair requirements.

6 Conclusions

Tunnel-form buildings are a type of RC structures commonly used in the construction of mass housing projects, specifically in seismically active regions, owing to their stiff and redundant structural characteristics. However, when characterised by a large number of stories (i.e., high-rise), they could exhibit heightened seismic vulnerability due to the presence of slender and lightly reinforced shear walls and conventionally reinforced squat coupling beams. The present paper investigates the seismic performance of a 14-storey tunnel-form building, selected for case-study purposes, and representative of typical constructions in Türkiye. A state-of-the-art finite element model in OpenSeesPY is created and extensively validated at both component- and system-levels. The building's component damage progression and system-level response are utilised to form a bespoke damage scale tailored for this building typology. Each damage state is defined based on the extent and distribution of structural and non-structural component damage across the structure. The damage scale is used in conjunction with non-linear time history analyses performed in a Multiple Stripe Analysis fashion to derive fragility curves. The procedure yielded 264 ground motion analyses, spanning a total of 12 levels of intensity measures.

The results show that inelastic deformations in shear walls commence at around 0.2% maximum inter-storey drift ratio, indicating the non-ductile behaviour of the building. The large number of shear walls per story significantly limits the lateral deformations and, therefore, constrains damage to the coupling beams until the damage is incurred in more shear walls more severely. In agreement with the findings from experimental campaigns, the analytical results indicate that the slender shear walls in the case study building exhibit brittle failure modes. While strain demands in the boundary and web reinforcement of shear walls gradually increase with the increasing intensity, failure of the concrete within the confined boundary region and unconfined web region occurs rapidly after exceeding a certain threshold. These observations demonstrate that lightly reinforced slender shear walls in the case study tunnel-form building experience rapid strength loss due to the failure of the compression zone. Furthermore, deterministic investigations reveal that coupled shear walls experience high levels of axial compression and tension forces, and they suffer from compression zone failure before yield commences in the coupling beams. On the one hand, this observation indicates the effectiveness of coupled systems in the load transfer mechanism. On the other hand, the delayed initiation of the yielding mechanism of the coupling beams suggests that coupling beams are ineffective in dissipating seismic energy, indicating that capacity design principles may be inadequate.

The performance assessment of the building indicates a high probability of meeting the life safety requirements, even in the event of very rare earthquakes. This attribute of the building primarily stems from the abundance of shear walls, which result in a redundant, stiff, and strong structure. However, immediate occupancy of the building is likely to be jeopardised in design-level ground motions. For events stronger than the design-level ground motions, significant repair costs and recovery times are expected, as the results indicate that the building is likely to experience substantial inelastic deformations in multiple shear walls and numerous coupling beams. The study allows the definition of fragility curves for each damage state defined in the bespoke damage scale. The median avgSa values for slight, moderate, extensive and near collapse are found to be 0.29 g, 0.36 g, 0.59 g, and 5.07 g, respectively. Furthermore, the median fragility parameters for $S_a(T_1)$ and PGA are also presented to facilitate the broader use of the results of this study.

The present study significantly advances knowledge on the seismic performance of high-rise tunnel form buildings. However, some limitations exist, and additional work is required to fill the research gaps. To generalise the results, additional studies on case study structures with other common configurations are required. Consideration of different heights is also needed to further investigate the impact of building height on the seismic performance of tunnel-form buildings. Lastly, additional post-earthquake field observations on the response and recovery of tunnel-form buildings are required to validate the proposed bespoke damage scale.

Appendix A: Engineering demand parameters for coupling beams

Table 8 shows EDP thresholds adopted for squat coupling beams in the case study building. As discussed in Chapters 2.2.2 and 3.1, the numerical model herein accurately represents the experimentally observed data. Accordingly, each squat coupling beam is analysed utilis-

Table 8 EDP thresholds for coupling beams in the case study building

Beam ID	EDP thresholds		
	$\theta_{cr}{}^{*}$ (rad)	$\theta_{0.9u}^{pre\ *}$ (rad)	$\theta_{0.8u}^{post*}$ (rad)
B01	0.00150	0.01000	0.02200
B02	0.00150	0.01300	0.05500
B03	0.00150	0.01400	0.02000
B04	0.00150	0.01500	0.04600
B05	0.00150	0.01300	0.02500
B08	0.00150	0.00650	0.03000

Note: *Determined from cyclic analysis of each coupling beam

ing the load patterns in the aforementioned studies (Breña and Ihtiyar 2011; Galano and Vignoli 2000; Kwan and Zhao 2002), and chord rotations presented in Table 8 is found to be the EDP thresholds defining coupling beam CLSs.

Appendix B: Estimates of fragility function parameters for different intensity measures

In this study, avgSa is adopted as the intensity measure due to its advantages, as elaborated in Chapter 4.1. In order to facilitate the broader benefit of the probabilistic performance assessment study conducted in this work, Table 9 presents the estimates of the median ($\hat{\theta}$) and logarithmic standard deviation ($\hat{\beta}$) for spectral acceleration at the fundamental period, $S_a(T_1)$, and peak ground acceleration, PGA, considering the prevalent use of these two intensity measures in ground motion prediction equations and seismic risk studies.

Table 9 Estimates of median ($\hat{\theta}$) and logarithmic standard deviation ($\hat{\beta}$) for different *IM-DS* pairs

Intensity Measure (g)	Damage State							
	Slight		Moderate		Extensive		Near Collapse	
	$\hat{\theta}$	$\hat{\beta}$	$\hat{\theta}$	$\hat{\beta}$	$\hat{\theta}$	$\hat{\beta}$	$\hat{\theta}$	$\hat{\beta}$
avgSa	0.2852	0.3001	0.3649	0.2574	0.5867	0.2705	5.0717	0.9077
$S_a(T_1 = 0.58\ s)$	0.3353	0.3498	0.4174	0.3081	0.6590	0.4976	36.3535	1.8555
PGA	0.1827	0.4846	0.2166	0.4582	0.3284	0.5946	11.2180	1.6340

Acknowledgements We acknowledge Professor Erdal Safak of the Earthquake Engineering Department at Kandilli Observatory and Earthquake Research Institute, Bogazici University, for making possible the ambient vibration measurements on the case study building and for his kind contributions, as well as technician Ahmet Korkmaz of the same department for his onsite support.

Author contributions All authors contributed to the conceptualisation of the study. Floor plans of the case study structure were obtained by Prof Hancılar. Finite element modelling, validations, record selection, finite element analyses, and assessments were conducted by Şahin Dede under the guidance of Prof Rossetto, Prof Freddi, and Prof Hancılar. The outline of the first draft was guided by Prof Rossetto and Prof Freddi, and the first draft of the manuscript was prepared by Şahin Dede. All authors commented on previous versions of the manuscript, and they read and approved the final manuscript.

Funding This work is part of the first author's PhD research, who is funded by the UCL Chadwick scholarship.

Data availability The datasets and codes generated during the presented study are available from the corresponding author on a reasonable request.

Declarations

Competing interests The authors have no relevant financial or non-financial interests to disclose.

References

American Concrete Institute (2011) Building code requirements for structural concrete (ACI 318-11) and commentary. In: ACI committee, vol 318. Farmington Hills

Ancheta TD, Darragh RB, Stewart JP, Seyhan E, Silva WJ, Chiou BSJ, Wooddell KE, Graves RW, Kottke AR, Boore DM, Kishida T (2014) NGA-West2 database. Earthq Spect 30(3):989–1005

ASCE (2010) Minimum design loads and associated criteria for buildings and other structures, ASCE/SEI 7-10. American Society of Civil Engineers, Reston, Virginia

Baker JW (2015) Efficient analytical fragility function fitting using dynamic structural analysis. Earthq Spect 31(1):579–599

Balkaya C, Kalkan E (2003) Nonlinear seismic response evaluation of tunnel form building structures. Comput Struct, 2003, 81(3):153–165

Balkaya C, Kalkan E (2004) Seismic vulnerability, behavior and design of tunnel form building structures. Eng Struct, 2004, 26(14):2081–2099

Behesthi Aval SB, Mohsenian V, Sadegh Kouhestani H (2018) Seismic performance-based assessment of tunnel form building subjected to near- and far-fault ground motions. Asian J Civ Eng 19:79–92

Beyer K, Dazio A, Priestley MJ (2008) Inelastic wide-column models for U-shaped reinforced concrete walls. J. Earthq. Eng 12(S1):1–33

Bianchini M, Diotallevi PI, Baker JW (2009) Prediction of inelastic structural response using an average of spectral accelerations. In: The 10th int conf on structural safety and reliability. Osaka, Japan. 13–17 Sept 2009

Birely AC (2012) Seismic performance of slender reinforced concrete structural walls. PhD Dissertation, University of Washington

Breña SF, Ihtiyar O (2011) Performance of conventionally reinforced coupling beams subjected to cyclic loading. J Struct Eng 137(6):665–676

CEN (2004) EN 1998–1 Eurocode, 8: design of structures for earthquake resistance-part, 1: general rules, seismic actions and rules for buildings. European Committee for Standardization, Brussels
Coleman J, Spacone E (2001) Localisation issues in force-based frame elements. J Struct Eng 127(11):1257–1265
Cordova PP, Deierlein GG, Mehanny SS, Cornell CA (2000) Development of a two-parameter seismic intensity measure and probabilistic assessment procedure. In The 2nd US-Japan Workshop on Performance-Based Earthquake Engineering Methodology for Reinforced Concrete Building Structures, Sapporo, Hokkaido, Japan. 11–13 Sep 2000
Dazio A, Beyer K, Bachmann H (2009) Quasi-static cyclic tests and plastic hinge analysis of RC structural walls. Eng Struct 31(7):1556–1571
Dede S, Gutiérrez-Urzúa F, Rossetto T, Freddi F (2024) Preliminary field observations of tunnel-form building damage from the February 2023 türkiye earthquakes. 18th. In World Conference on Earthquake Engineering, Milan, Italy, 30th June - 5th July 2024
Deger ZT, Wallace JW (2015) Collapse assessment of the alto rio building in the 2010 Chile earthquake. Earthq Spect 31:1397–1425
Ding R, Tao MX, Nie JG, Mo YL (2016) Shear deformation and sliding-based fiber beam-column model for seismic analysis of reinforced concrete coupling beams. J Struct Eng 142(7):04016032
Elwood KJ (2013) Performance of concrete buildings in the 22 February 2011 Christchurch earthquake and implications for Canadian codes. Canadian J Civ Eng 40:759–776
Federal Emergency Management Agency (FEMA) (2018) Seismic performance assessment of buildings (FEMA P-58). FEMA, Washington, DC
Filippou FC, Popov EP, Bertero VV (1983) Effects of bond deterioration on hysteretic behavior of reinforced concrete joints. Earthq eng research center. Report to the National Science Foundation, No. UCB/EERC-83/19
Freddi F, Ghosh J, Kotoky N, Raghunandan M (2021) Device uncertainty propagation in low-ductility RC frames retrofitted with BRBs for seismic risk mitigation. Earthq Eng & Struct Dyn 50(9):2488–2509
Galano L, Vignoli A (2000) Seismic behavior of short coupling beams with different reinforcement layouts. ACI Struct J 97(6):876–885
Gallardo JA, De La Llera JC, Santa María H, Chacón MF (2021) Damage and sensitivity analysis of a reinforced concrete wall building during the 2010, Chile earthquake. Engin Struct 240:112093
Gogus A, Wallace JW (2015) Seismic safety evaluation of reinforced concrete walls through FEMA P695 methodology. J Struct Eng 141(10):04015002
Grünthal G (1998) European macroseismic scale 1998 EMS-98. Centre Europèen de Géodynamique et de Séismologie, Luxembourg
Haselton CB, Whittaker AS, Hortacsu A, Baker JW, Bray J, Grant DN (2012) Selecting and scaling earthquake ground motions for performing response-history analyses. 15*th*. In: World conf of Earthq Eng. Lisbon. 24–28. Sept 2012
Hazus, FEMA (2022) Hazus earthquake model technical manual-hazus 5.1. Federal emergency management agency. Washington, DC, USA
Housing Development Administration of the Republic of Türkiye (TOKİ) (2022) Housing programs. January 15 – Retrieved September 13, 2024. https://www.toki.gov.tr/en/housing-programs.html
Jalayer F (2003) Direct probabilistic seismic analysis: implementing nonlinear dynamic assessments. PhD dissertation, Stanford University, CA, USA
Ji X, Liu D, Sun Y, Molina Hutt C (2017) Seismic performance assessment of a hybrid coupled wall system with replaceable steel coupling beams versus traditional RC coupling beams. Earthq Eng & Struct Dyn 46(4):517–535
Jünemann R, De la Llera JC, Hube MA, Cifuentes LA, Kausel E (2015) A statistical analysis of reinforced concrete wall buildings damaged during the 2010, Chile earthquake. Engin Struct 82:168–185
Kalkan E, Yüksel SB (2008) Pros and cons of multistory RC tunnel-form (box-type) buildings. The Struct Design Of Tall And Special Buildings, 2008, 17(3):601–617
Kam WY, Pampanin S, Elwood K (2011) Seismic performance of reinforced concrete buildings in the 22 February Christchurch (Lyttelton) earthquake. Bull New Zealand Society Earthq Eng 44:239–278
Kaya Y, Şafak E (2015) Real-time analysis and interpretation of continuous data from structural health monitoring (SHM) systems. Bulletin Earthq Eng 13:917–934
Kazantzi AK, Vamvatsikos D (2015) Intensity measure selection for vulnerability studies of building classes. Earthq Eng & Struct Dyn 44(15):2677–2694
Kohrangi M, Bazzurro P, Vamvatsikos D, Spillatura A (2017) Conditional spectrum-based ground motion record selection using average spectral acceleration. Earthq Eng & Struct Dyn 46(10):1667–1685
Kwan AK, Zhao ZZ (2002) Cyclic behaviour of deep reinforced concrete coupling beams. In Proceedings of the Institution of Civil Engineers - Structures and Buildings, vol 152(3): 283–293

Lee HS, Hwang KR (2013 Sept 8–12) Effect of slabs on the seismic response of a three dimensional wall-type building structure. In: The 2013 world congress on advances in struct eng & mechanics. Jeju, Korea
Lemnitzer A, Massone LM, Skolnik DA, De La Llera Martin JC, Wallace JW (2014) Aftershock response of RC buildings in Santiago, Chile, succeeding the magnitude 8.8 Maule earthquake. Eng Struct 76:324–338
Li S, Jiang H, He L (2019) Study of a new type of replaceable coupling beam in reinforced concrete shear wall structures. The Structural Design Of Tall And Special Buildings 28(10):e 1620
Luco N, Cornell CA (2007) Structure-specific scalar intensity measures for near-source and ordinary earthquake ground motions. Earthq Spect 23(2):357–392
Mander JB, Priestley MJ, Park R (1988) Theoretical stress-strain model for confined concrete. J Struct Eng 114(8):1804–1826
Massone LM (2013) Fundamental principles of the reinforced concrete design code changes in Chile following the M_w 8.8 earthquake in 2010. Engin Struct 56:1335–1345
Mehanny SS (2009) A broad-range power-law form scalar-based seismic intensity measure. Eng Struct 31(7):1354–1368
Ministry of Public Works and Settlement (2007) Turkish Building Seismic Code (2007): regulations for buildings to be built in seismic zones. Ministry of Public Works and Settlement, Ankara
Moehle JP (2015) Seismic design of reinforced concrete buildings, vol 814. McGraw-Hill Education, New York
Mohsenian V, Di Sarno L (2024) Numerical analysis of potential failure modes in shear walls of the tunnel form concrete system: performance-based approach. Engin Struct 303:117494
Mohsenian V, Gharaei-Moghaddam N, Moghadam AS (2024) Evaluation of slab-wall connections in tunnel form concrete structures: a multi-level approach based on seismic demand and capacity. Eng Fail Analysis 156:107833
Mohsenian V, Mortezaei A (2019) New proposed drift limit states for box-type structural systems considering local and global damage indices. Advances In Struct Eng 22:3352–3366. https://doi.org/10.1177/1369433219863299
Mohsenian V, Nikkhoo A, Rostamkalaee S, Moghadam AS, Hejazi F (2021) The seismic performance of tunnel-form buildings with a non-uniform in-plan mass distribution. Structures 29:993–1004
Odabasi O, Kohrangi M, Bazzurro P (2021) Seismic collapse risk of reinforced concrete tall buildings in Istanbul. Bull Earthq Eng 19:6545–6571
Pugh JS, Lowes LN, Lehman DE (2015) Nonlinear line-element modeling of flexural reinforced concrete walls. Eng Struct 104:174–192
Ramos L, Hube MA (2021) Seismic response of reinforced concrete wall buildings with nonlinear coupling slabs. Engin Struct 234:111888
Republic of Türkiye Ministry of Environment and Urbanization (2018) Turkish Building Seismic Code (2018): regulations for buildings to be built in seismic zones. Ministry of Environment and Urbanization, Ankara
Rossetto T, Gehl P, Minas S, Galasso C, Duffour P, Douglas J, Cook O (2016) FRACAS: a capacity spectrum approach for seismic fragility assessment including record-to-record variability. Eng Struct 125:337–348
Rossetto T, Ioannou I, Grant DN, Maqsood T (2014) Guidelines for empirical vulnerability assessment. GEM technical report 2014–08 V1.0.0, GEM Foundation, Pavia, Italy, p 140
Şafak E, Çakti E (2014) Simple techniques to analyse vibration records from buildings. In The 7th European Workshop on Structural Health Monitoring, Nantes, France. 8th Jul 2014
Şafak E, Çaktı E, Kaya Y (2010) Recent developments on structural health monitoring and data analyses. In: Garevski M, Ansal A (eds.) Earthq Eng in Europe. Geotech, Geological, and Earthq Eng, vol 17. Springer, Dordrecht
Scott MH (2011) Numerical integration options for the force-based beam-column element in OpenSees. Force-based element integration options in OpenSees 1–7. 26 Jan, 2011
Sönmez E, Rodriguez ME (2024) Frame buildings are not an answer for earthquakes: the case of the February 2023 earthquakes in Türkiye. Earthq Spect 40(4):2364–2382
Tavafoghi A, Eshghi S (2013) Evaluation of behavior factor of tunnel-form concrete building structures using applied technology council 63 methodology. Struct Des Tall Spec Build 22:615–634
Ugalde D, Parra PF, Lopez-Garcia D (2019) Assessment of the seismic capacity of tall wall buildings using non-linear finite element modeling. Bull Earthq Eng 17:6565–6589
Vamvatsikos D, Cornell CA (2005) Developing efficient scalar and vector intensity measures for IDA capacity estimation by incorporating elastic spectral shape information. Earthq Eng & Struct Dyn 34(13):1573–1600
Wallace JW, Massone LM, Bonelli P, Dragovich J, Lagos R, Lüders C, Moehle J (2012) Damage and implications for seismic design of RC structural wall buildings. Earthq Spect 28:281–299

Westenenk B, De la Llera JC, Besa JJ, Jünemann R, Moehle J, Lüders C, Inaudi JA, Elwood KJ, Hwang SJ (2012) Response of reinforced concrete buildings in Concepción during the maule earthquake. Earthq Spect 28:257–280

Yakut A, Gulkan P (2003) Housing report tunnel form building. Earthquake Engineering Research Institute (EERI) and International Association for Earthquake Engineering (IAEE), turkey/Report. 2003 Oct 15, 101

Yüksel SB, Kalkan E (2007) Behavior of tunnel form buildings under quasi-static cyclic lateral loading. Struct Eng & Mechanics, 2007, 27(1):99

Zhu M, McKenna F, Scott MH (2018) OpenSeesPy: python library for the OpenSees finite element framework. SoftwareX 7:6–11